Kalman Filter-Based Systems Approach for Prognostics and Health Management of Electric Motors

Hyung Jun Park, Dongwoo Lee, Seokgoo Kim, Nam Ho Kim, and Joo-Ho Choi

Abstract A Kalman filter-based framework is proposed for the prognostics and health management of DC electric motors by treating them as a system. The control signals of the motor are used to estimate the current health and predict the remaining useful life (RUL) of the motor and its components, such as bearings and permanent magnets. The framework consists of an online health diagnosis to estimate the health status of the motor and each component, and an offline failure prognosis to predict the RULs. The approach is demonstrated with the aid of two real examples: the reaction wheel motor for advanced attitude control of satellites and the driving motors in a quadcopter to lift and control flight operations. In each example, the motors were subjected to accelerated degradation tests, motor control data were collected for each cycle, and RULs were predicted against failure thresholds critical to motor performance. The results showed that the framework can be used to effectively predict the RUL of a degraded motor, thereby enabling failure prevention and proactive maintenance scheduling.

H. J. Park
Department of Aerospace and Mechanical Engineering, Korea Aerospace University, Gyeong gi-do 10540, Republic of Korea

D. Lee
D&SHINE Research Institute, Gyeong gi-do 10540, Republic of Korea

S. Kim · N. H. Kim
Department of Mechanical and Aerospace Engineering, University of Florida, Gainesville, FL 32611, USA

J.-H. Choi (✉)
School of Aerospace and Mechanical Engineering, Korea Aerospace University, Gyeong gi-do 10540, Republic of Korea
e-mail: jhchoi@kau.ac.kr

© The Author(s), under exclusive license to Springer Nature Switzerland AG 2023

Y. Liu et al. (eds.), *Advances in Reliability and Maintainability Methods and Engineering Applications*, Springer Series in Reliability Engineering,
https://doi.org/10.1007/978-3-031-28859-3_21

1 Introduction

The accurate prediction of impending failure or remaining useful life (RUL) of mission-critical systems improves safe system operations and offers economic benefits to the industry. Extensive research on the prognostics and health management (PHM) of various assets with different perspectives has already been conducted by academic researchers and industrial engineers [1, 2]. Among these, the PHM of electric motors has been widely researched because of its ability to provide the drive and control of various equipment and processes in the industry. To conduct PHM, motor current or vibration signals are typically employed to assess and predict the health of a motor [3]. Traditionally, the failure modes of a motor have been identified by time and frequency analyses of the signals, such as by estimating the harmonic components of the fault frequencies and locating them in the spectrum [4–7]. Currently, artificial intelligence (AI)-based approaches, which are known to be powerful and possess improved performance over the conventional approaches, are widely adopted. These approaches consist of classification tools and algorithms, such as neural networks [8], fuzzy logic [9], support vector machines [10], and deep learning [11]. A general review of AI-based approaches for electric motors is presented in Ref. [12].

Most engineering systems consist of multiple components designed to perform a specific function. Because these components interact with each other in a complex manner, their degradation can affect the overall system performance in a non-trivial way. Recently, an appropriate framework that estimates the health of the components and predicts their RUL was proposed by Kim et al. [13, 14]. They also demonstrated the framework using a DC motor, considering it as a system because it has mechanical parts, that is, the bearing, shaft, and electrical components such as the stator winding and magnets. Because the performance degradation of the motor originates from these components, it is desirable to employ a systems approach to implement the PHM for motors. The framework consists of online diagnostics to monitor the status of each component and the overall health of the motor, as well as an offline failure prognosis to predict the RULs against the failure threshold conditional on motor performance.

Prognostic methods applied in PHM can be categorized into model-based and data-driven approaches. The model-based approach assumes that a physical model describing the behavior of the system is available and combines the model with measured data to identify the model parameters. Conversely, the data-driven approach uses data from past failures to establish a prediction model based on machine learning. The model-based approach is advantageous for DC motors because it is a dynamic model that enables estimation of the model parameters using the measured signals, which are indicative of the component's health. Hence, several researchers have applied model-based approaches to the PHM of DC motors. In this approach, the Kalman filter (KF) is the most widely used technique for estimating the model parameters in a recursive manner while incorporating the model and measurement uncertainties. Rahimi et al. [15] applied an unscented KF with a high-fidelity model to estimate health parameters for each motor fault scenario. El Sayed et al. [16] performed

parameter estimation using an extended KF (EKF) and an unscented KF (UKF) to diagnose stator faults and their severity. Others, such as Singleton et al. [17], used a KF to estimate motor speed and conducted fault detection based on a comparison with the actual speed. However, a common drawback of the aforementioned studies is that no one has explored the systems approach, wherein the RUL prediction accounts for component degradation and their influence on the overall motor performance.

This section addresses the application of the systems approach, in which the KF is used with motor-current signals to estimate the present health status of individual components and performance degradation. The advantages of the systems approach are two-fold. First, it does not require large volume of data until failure, which is critical to the training process in the data-driven approach. Second, additional sensors, such as accelerometers, are not required because the motor load current signal, which is acquired during operation, is used for the PHM. In Sect. 2, the overall prognostics framework for the systems approach is reviewed briefly. In Sect. 3, simulations are conducted using the motor dynamic equations in which the two most critical components, that is, the permanent magnet and bearing, are artificially degraded over cycles, and virtual measurements are performed accordingly to illustrate the process of RUL prediction. Next, two case studies of real motors are presented to demonstrate their implementation. The first is presented in Sect. 4, which considers the degradation of the reaction wheel (RW) motor, which stabilizes the attitude control of satellites against external environmental factors. The second is presented in Sect. 5 for the motors driving the quadcopter to lift and control flight operations. In both examples, the motors were subjected to accelerated degradation and the motor-current signals were collected with regular time interval during operation. A systems approach is employed wherein the performance of the motor is properly defined. The health of each motor component is assessed based on this, and the RUL, after which the motor is no longer able to perform its normal function, is predicted. In Sect. 6, a detailed discussion and conclusions are presented.

2 Systems Approach for PHM

The overall framework of the systems approach for fault diagnosis and failure prognosis based on a physical model-based approach is described in this section. Figure 1 describes the framework which consists of two phases: construction of the system dynamics model on the left and the PHM implementation on the right.

The system model is developed using simulation tools or algorithms such as Simulink, lumped parameters, or ordinary differential equations. A group of parameters is identified during development; the inputs are the operation parameter u and the health parameter h of the critical components that affect system degradation. The outputs are the state variable x, the system performance variable S, and the measurement variable z used to estimate the present health status of the system and its components. Three models are established: the state model—typically in a recursive form in the time domain—the measurement model relating the state with

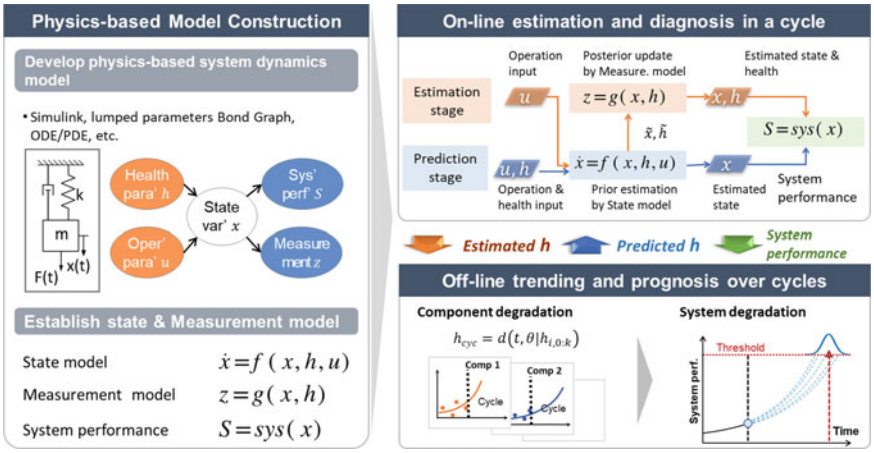

Fig. 1 Framework for physics-based approach [13]

the measurement, and the performance model of the system. The three models are defined as follows:

$$\dot{x} = f(x, h, u), \tag{1}$$

$$z = g(x, h), \tag{2}$$

$$S = sys(x). \tag{3}$$

The PHM implementation phase consists of two parts: online estimation and diagnosis in the upper-right figure, as well as offline training and prognosis in the lower-right figure. In the online estimation, state x in a single cycle is estimated for the input operation parameter u, from which the system performance S is evaluated using the performance model. Depending on the availability of health parameter h, the online estimation phase comprises two stages. In the estimation stage, h and x are estimated as unknowns using the measured data z. The unknown parameters are estimated by the state model and updated by the measurement model. In the prediction stage, h is known as a priori and there are no measurements; in this case, state x is predicted with the given input h. In both stages, the system performance is computed using the obtained state x. Using the measurement z obtained in every cycle, the health parameters up to the current cycle k, i.e., $h_{0:k}$, can be estimated. They are then transferred to offline training and prognosis. To describe the degradation trend more efficiently, the health parameters are typically represented by either a physical model or an empirical model:

$$h_{cyc} = d(t, \theta|h_{0:k}), \tag{4}$$

where h_{cyc} denotes the health parameters as a function of cycles, d is the mathematical model, θ is the model parameter, and t is the cycle. Once the model is fitted to $h_{0:k}$, it can be extrapolated to predict h in the future. The predicted h is transferred to the prediction stage from which state x and the system performance S in the future are predicted. The predicted S is transferred to the offline training phase to obtain the future evolution of the system performance, as matched with that of the health parameter h in the future. Upon evaluating the RUL of the system performance against the failure threshold, one can identify the most critical health parameter (i.e., specific component) that leads to the earliest system failure and its remaining cycles, which provides valuable information in maintenance management.

The overall procedure is illustrated in Fig. 2. For the implementation phase, the online estimation and diagnosis part of Fig. 1 can be best accommodated by a Bayesian approach, such as the Extended Kalman or Particle Filter algorithms. Thereafter, the health parameter h and state x are estimated in the form of a distribution, such as the mean and covariance, or the samples which reflect the uncertainty in the process. The offline training and prognosis parts can also be similarly performed; however, a simpler linear/nonlinear regression can also be employed to this end. The degradation model parameter θ in $d(\cdot)$ is estimated based on the accumulated values $h_{0:k}$ until the current cycle. The degradation in the future is then predicted by θ with uncertainty, which is usually expressed by the confidence bounds in the result.

Construction phase (left figure)	
• Establish state, measurement, and performance model, as given in (1)-(3)	
Implementation phase (right figure)	
• Estimate health parameter h and state x using the measurement z.	Estimation stage in upper figure
• Transfer estimated data $h_{0:k}$ up to the current cycle to offline trending.	
• Fit the data $h_{0:k}$ to degradation model (4) and extrapolate h to predict the future degradation.	Left part of lower figure
• Transfer predicted health parameters h in the future to online estimation.	
• Predict state x and system performance S using h in the future.	Prediction stage in upper figure
• Transfer predicted S in the future to offline trending.	
• Determine the remaining life of S against failure threshold.	Right part of lower figure

Fig. 2 Overall procedure for physics-based approach as illustrated

3 Simulation Study

3.1 Problem Statement

In this section, the simulation data are used to illustrate the system approach procedure for a DC motor. Most of the contents here are extracted from the authors' previous study [13]. Virtual measurement data are generated by adding random noise to the simulation results of the motor dynamics that converts electrical energy into mechanical power. When an electric current passes through a coil in a magnetic field, the magnetic force produces torque that drives the DC motor. As shown in Fig. 3, a DC motor consists of electrical and mechanical parts that are coupled together; failure in one part affects the others. For example, because magnetic flux enables conversion of electrical energy into mechanical force, its defects can degrade mechanical performance. The mechanical and electrical parts of the DC motor dynamics are expressed as:

$$J\frac{d\omega}{dt} + b\omega = k_T i - T_L = T_o, \tag{5}$$

$$L\frac{di}{dt} + Ri = V - k_T\omega, \tag{6}$$

where ω, i, and T_o represent the angular velocity, current, and output torque, respectively. The two equations share the common parameter k_T, which represents the electromechanical coupling coefficient, and Table 1 lists the parameters and their values used for the simulation [18]. The duration of a single cycle is 3 s, and a voltage of 10 V is applied for the first 1.5 s and subsequently turned off. Figure 4 shows the time histories of ω, i, and T_o as outputs from the dynamic equations in (5) and (6), respectively. The angular velocity ω rapidly reached the desired value on application of power and decreased to zero when turned off. Similarly, load current i and output torque T_o rapidly increased to the peak value at the start, followed by a gradual decrease when the voltage was turned off.

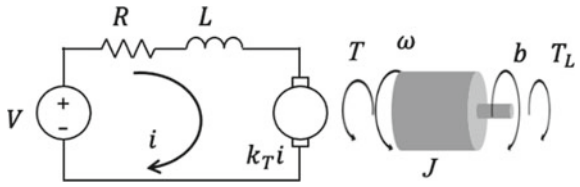

Fig. 3 DC motor system

Table 1 Parameter setting for simulation

Symbol	Description	Value
R	Armature resistance	11.2
L	Armature inductance	0.1215 H
J	Moment of inertia	0.022145 kg m^2
b	Viscous friction coefficient	0.002953 N m s/rad
k_T	Electromechanical coupling coefficient	1.28 Nm/A
V	Input voltage	10 V
T_L	Load torque	0.05 Nm

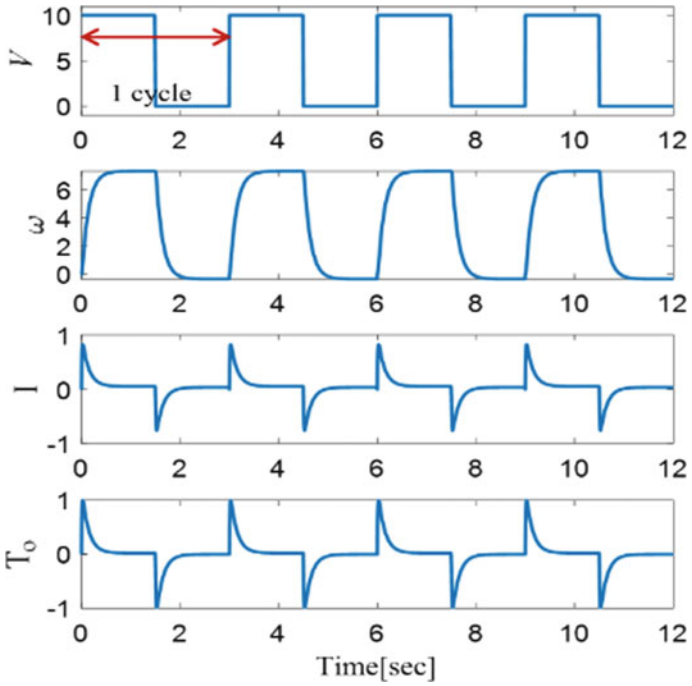

Fig. 4 Simulation result of DC motor system

3.2 Simulation of Component Degradation

Challenges with system-level prognosis arise because multiple components degrade over time, which affect system performance in a complex manner. To simulate this situation, two components with associated failure modes were selected from [19]. The first is degradation of the permanent magnet owing to prolonged overheating, also called flux weakening, that results in reduction of rotor magnetic-field strength. This can be described by decreasing the electromechanical coupling coefficient,

k_T. The second is bearing lubrication failure, which can be modeled by a change in the load torque T_L applied to the motor. The system performance is given by the motor output torque T_o, which may decrease as the two components degrade. The degradation behaviors of the magnet and bearing are assumed to be linear and exponential functions of the cycles, respectively.

$$k_T(t) = \alpha_1 + \alpha_2 t, \tag{7}$$

$$T_L(t) = \beta_1 e^{\beta_2 t}, \tag{8}$$

where α_1 and β_1 represent the initial degraded status, and α_2 and β_2 describe the cycle-dependent behavior.

Three cases are considered, as shown in Fig. 5: (1) degradation of the magnet with $\alpha_2 = -5.7974 \times 10^{-4}$, (2) degradation of the bearing with $\beta_2 = 3.3 \times 10^{-3}$, and (3) simultaneous degradation with the $\alpha_2 = -5.7974 \times 10^{-4}$ and $\beta_2 = 3.9 \times 10^{-3}$. The output torque for each case was obtained by solving the system equations with the degraded values of k_T and T_L, as shown in Fig. 5a–e; results for the output torque are presented in Fig. 5b, d, and f. It can be observed that the maximum value of the output torque gradually decreases with degradation, thereby indicating degradation of the system performance. Furthermore, it is evident from Fig. 5b, d, and f that when two or more components degrade simultaneously, the system performance degrades at a faster rate.

In this example, the system performance S is defined by a scalar value, namely the maximum output torque:

$$S = \max T_0 = \max(k_T i - T_L). \tag{9}$$

A system is regarded as a failure when the system performance decreases below 70% of its initial value. Therefore, it is necessary to predict the number of cycles that remain before failure, as well as the responsible component to be replaced.

3.3 Application of Physics-Based Approach

As mentioned in the previous section, the first step in the physics-based approach is construction of the system dynamics model, as shown in (1), where the state variable $\boldsymbol{x}$ (denoted by a vector hereafter) consists of velocity ω and current i, that is, $\boldsymbol{x} = [\omega, i]^T$ while the input operation parameter u is voltage V. The health parameter $\boldsymbol{h}$ contains k_T and T_L or $\boldsymbol{h} = [k_T, T_L]^T$. The state model can be constructed using (5) and (6) as follows:

$$\begin{bmatrix} \dot{\omega} \\ i \end{bmatrix} = \begin{bmatrix} -\frac{b}{J} & \frac{k_T}{J} \\ \frac{k_T}{L} & -\frac{R}{L} \end{bmatrix} \begin{bmatrix} \omega \\ i \end{bmatrix} + \begin{bmatrix} \frac{T_L}{J} \\ \frac{V}{L} \end{bmatrix}. \tag{10}$$

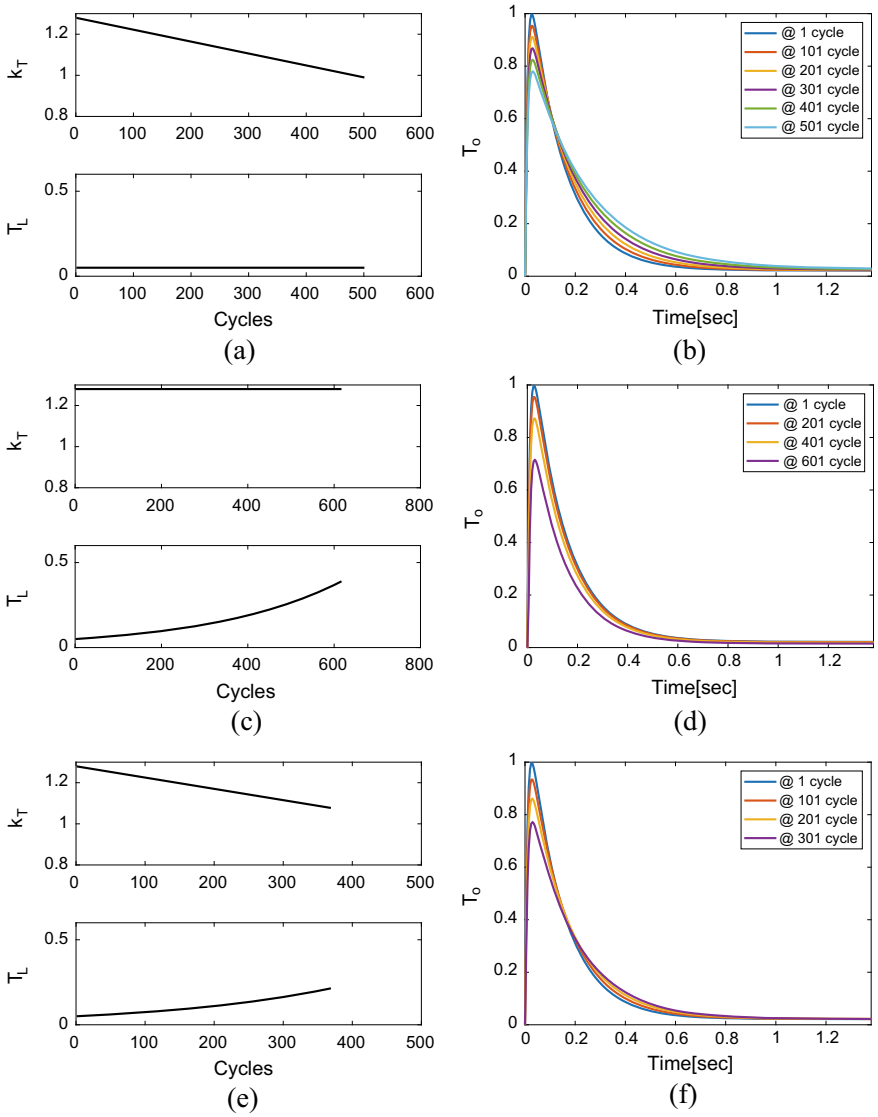

Fig. 5 Output torque due to components degradation, **a** health parameters and **b** output torque of case 1, **c** health parameters and **d** output torque of Case 2, and **e** health parameters and **f** output torque of Case 3

Note that the equation describes the transient response of the state variable $\boldsymbol{x}$. Because the state variable can be acquired from the control unit during operation, the measurement model is expressed as:

$$z = \begin{bmatrix} 1 & 0 \\ 0 & 1 \end{bmatrix} \begin{bmatrix} \omega \\ i \end{bmatrix} + \boldsymbol{v}, \tag{11}$$

where z is the measurement variable, and $\boldsymbol{v}$ is the zero-mean multivariate Gaussian noise. The measurement data were gathered at 0.005 s time intervals.

The models were used for online estimation and diagnosis. In this study, an EKF algorithm was employed. In the estimation stage, the state variable is augmented by the unknown health parameter $\boldsymbol{h}$ and denoted by $\mathbf{x} = \left[\boldsymbol{x}^T, \boldsymbol{h}^T\right]^T$. The state and measurement models in (10) and (11) can be rewritten in recursive matrix form:

State model: $\mathbf{x}_t = F(\mathbf{x}_{t-1}) + \boldsymbol{w}_t$ or

$$\begin{bmatrix} \omega_t \\ i_t \\ k_{T,t} \\ T_{L,t} \end{bmatrix} = \begin{bmatrix} (1 - b \cdot dt/J)\omega_t + dt/J\left(k_{T,t-1} \cdot i_{t-1} - T_{L,t-1}\right) \\ -dt/L \cdot k_{T,t-1} \cdot \omega_{t-1} + \left(1 - \frac{R}{L}\right) i_{t-1} + V \cdot dt/L \\ k_{T,t-1} \\ T_{L,t-1} \end{bmatrix} + \boldsymbol{w}_t. \tag{12}$$

Measurement model: $z_t = H(\mathbf{x}_t) + \boldsymbol{v}_t$ or

$$z_t = \begin{bmatrix} 1 & 0 & 0 & 0 \\ 0 & 1 & 0 & 0 \end{bmatrix} \begin{bmatrix} \omega_t \\ i_t \\ k_{T,t} \\ T_{L,t} \end{bmatrix} + \boldsymbol{v}_t, \tag{13}$$

where $k_{T,t}$ and $T_{L,t}$ denote the k_T and T_L at the current time t, respectively. Process error $\boldsymbol{w}_t$ is given by the zero-mean multivariate Gaussian noise with covariance, whose diagonal elements are $I \times 10^{-9}$, where I is the identity matrix. The measurement noise $\boldsymbol{v}_t$ is set as 0.1 and 0.01, which can be determined by evaluating the dispersion of the measured data. More details on the EKF can be found in literature [17, 20].

The initial state variables are given as $\mathbf{x}_0 = [0, 0, 1.28, 0.05]^T$ based on the evaluation of k_T and T_L at the initial stage of motor operation. The estimation stage was performed in two steps, as shown in Fig. 1. The first is prior estimation by the state model under a given input $\boldsymbol{u}$. Next is the posterior update by the measurement model, which leads to the estimated state variable and health parameters. Figure 6a, b show the estimated state variable $\boldsymbol{x}$ (velocity and current) and health parameters $\boldsymbol{h}$ (k_T and T_L) along with 95% prediction and confidence intervals, respectively. As shown in Fig. 6b, the health parameters rapidly converged to their true values. The values at the end of the voltage application (i.e., 1.5 s) were used as the estimated health of each component to assess the system performance given by (9).

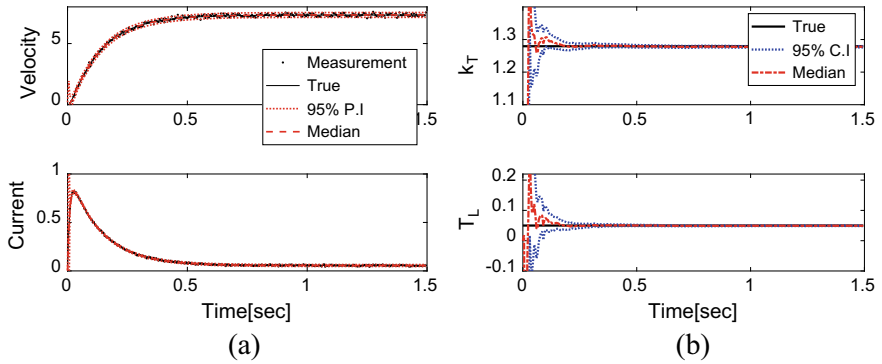

Fig. 6 Online estimation and diagnosis in a cycle by physics-based approach: **a** state variable $\boldsymbol{x}$ and **b** health parameters h

Once the health parameters $\boldsymbol{h}$ are estimated for each cycle, the next step is to transfer them to the offline stage, as shown in Fig. 1. The results are shown in Fig. 7a, c, and e for all three cases; the black dots denote health parameters estimated up to the current cycle. Using these data, the degradation models of each health parameter were fitted, i.e., the model parameters $\boldsymbol{\alpha}$ and $\boldsymbol{\beta}$ in (7) and (8) were estimated. For this purpose, the Markov Chain Monte Carlo (MCMC) method, which determines the parameters by large samples (10^4 in this study) to represent the uncertainty, is applied for the likelihood between the data and the model. Future degradation behaviors were also predicted by extrapolating the model. In Fig. 7a, c, and e, these are represented by the median and 95% predictive interval (PI) curves. Note that the associated uncertainty is so small that it nearly overlaps in this example. Once the health parameters $\boldsymbol{h}$ are predicted for future cycles, they are transferred to the online stage, as shown in Fig. 1. In this case, they are used for the prediction stage wherein only the state variables $\boldsymbol{x}$ are estimated by the state model, because $\boldsymbol{h}$ is known. Subsequently, the system performance in the future cycles obtained as samples are transferred to the offline prognosis over cycles. The results are given by the median and 95% PI in Fig. 7b, d, and f for the three cases, respectively. It is worth noting that establishing a degradation model for the system performance is not necessary because these are obtained from the online estimation stage as samples.

Because true solutions are available, they are superimposed by solid black lines and compared with the predictions. The prediction results at the current cycle agree well with the true solutions for all three cases. It should be noted that the system failure is defined as 70% of its initial value, depicted by the horizontal green line in the figure. The end of life (EOL) was found at 683, 617, and 369 cycles in terms of the median for the three cases. The reason for the shorter life in Case 3 is attributed to the acceleration effect caused by the simultaneous degradation of both components. In Fig. 7a, c, and e, the blue dotted horizontal lines indicate the failure thresholds of each health parameter. They are defined by the corresponding values at EOL when

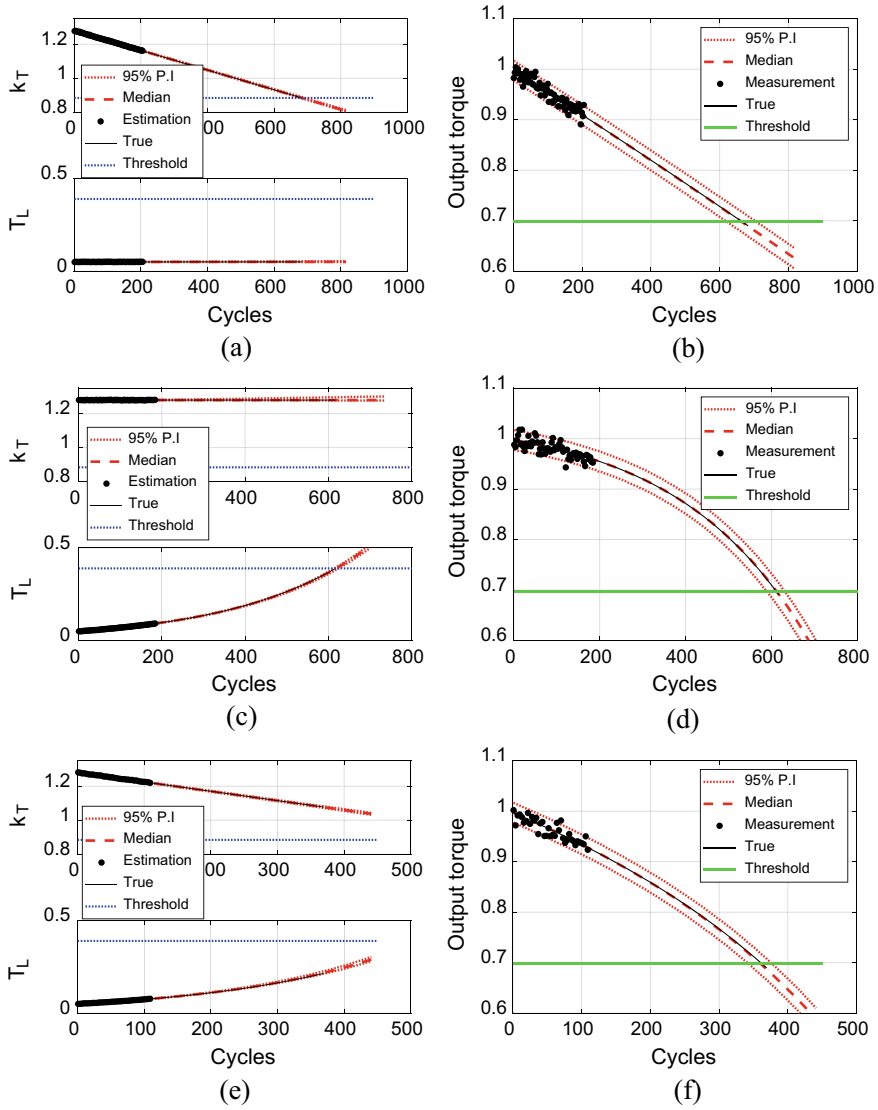

Fig. 7 Offline trending and prognosis over cycles by physics-based approach: **a** components health degradation for Case 1, **b** system health degradation for Case 1, **c** components health degradation for Case 2, **d** system health degradation for Case 2, **e** components health degradation for Case 3 and **f** system health degradation for Case 3

the system undergoes degradation of each component. The threshold values for k_T and T_L are 0.884 and 0.3897 at EOLs 683 and 617 from cases 1 and 2, respectively.

Once the system prognostics information is available, the maintenance effect of individual components on the system health can be evaluated. This process is illustrated in Case 3 wherein two components degrade simultaneously. Note that all subsequent computations are based on median values, unless stated otherwise. First, the current conditions are assessed by introducing the health index (HI) and RUL. The HI indicates the current health status, whereas the RUL estimates how many cycles remain until final failure. HI is defined by the ratio of degradation at the current cycle to that at the EOL and ranges from 0 (normal) to 1 (failure). Because the k_T values at the initial, current, and EOL cycles are 1.28, 1.1, and 0.88, respectively (Fig. 7a), the index is $(1.28 - 1.10)/(1.28 - 0.88) = 0.45$. The indices for the other parameters can be obtained in a similar manner. RUL is defined as the difference between EOL and the current cycle. For k_T and T_L in Fig. 7e, the EOLs are found at the cycles crossing the threshold lines (not shown here), which are approximately 721 and 513, respectively. Because the current cycle is 109, the RULs of k_T and T_L are approximately 609 and 412, respectively, and the system RUL is $361 - 109 = 252$ cycles.

All the results are summarized in Table 2 and plotted using bar charts in Fig. 8a, b. Note in Table 2 that the HI of k_T has degraded (increased) to 0.1507, which is greater (worse) than the 0.0789 of T_L. However, its RUL is approximately 609, which is longer than the 412 of T_L. This is because of their different degrees of influence on the overall system performance.

Subsequently, a what-if study was performed for scenarios in which one of the components was repaired or replaced by a new one. The health parameter is reset to the original value and the system performance is predicted under the renewed condition when the components that influence the health are replaced. These results are shown in Fig. 8c, d when the components that influence factors k_T and T_L are repaired. The new EOLs of the components that influence factors k_T and T_L got extended to approximately 512 and 701 cycles, respectively, thereby yielding new RULs of approximately 403 and 592, respectively, as shown in Fig. 8d. Among the choices regarding which component to repair, repairing the bearing (T_L) is more

Table 2 Results for simulation

Name	Flux	Bearing	System performance
Symbol	k_T	T_L	S
Current cycle	109	109	109
End of life	718.0811	521.1807	361
Remaining useful life	609.0811	412.1807	252
Initial value	1.2796	0.05	0.9971
Current value	1.22	0.0768	0.9278
Threshold	0.884	0.3897	0.6978

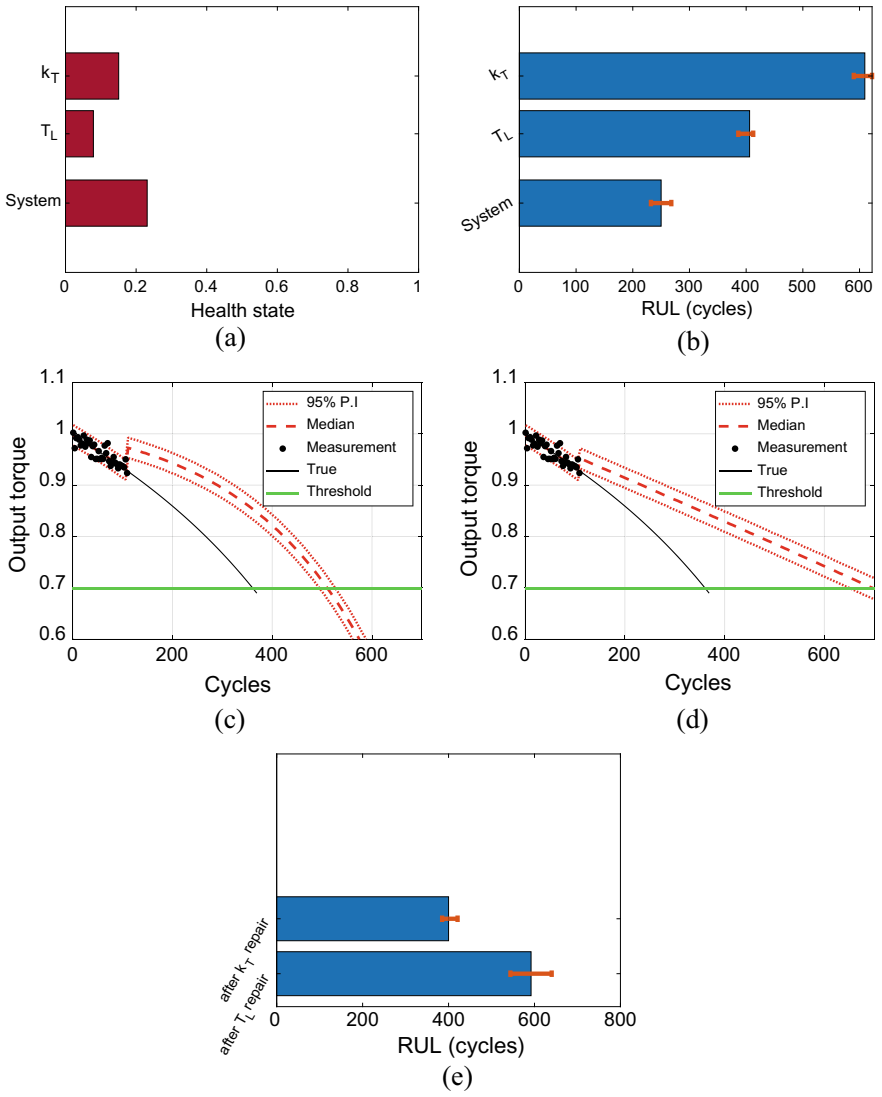

Fig. 8 Maintenance scenario in physics-based approach: **a** current health status, **b** RUL of component and system, **c** prognosis with k_T repair, **d** prognosis with T_L repair and **e** system RUL when component is repaired

desirable as it leads to a longer RUL. In Fig. 8b, e, the red error bar indicates the 95% PI of the RUL prediction. Answers to the following significant questions could be found from this study: what is the current health condition of the components and system, how much longer can the system operate until failure, which component

should be replaced to extend the system life, and how much longer can the system operate after repair.

In the following section, two real-world examples are addressed to illustrate the applications of the proposed framework: motors for the attitude control of satellites and driving quadcopters.

4 Case Study 1: Reaction Wheel Motor in Satellites

4.1 Problem Definition

In this section, reaction wheel motors for the attitude control of satellites are considered. Note that the most of the contents in this case study are from the authors' previous paper [21]. Satellites in space require accurate attitude control and high reliability to conduct their missions fully. The RW actuated by a motor provides consistent angular momentum to help stabilize a satellite against external torsion, such as solar radiation pressure, and to control its precise attitude. However, owing to continuous operation, the functioning of the motor becomes degraded over time, thereby jeopardizing the reliability of the entire satellite control system [22]. According to a survey of the failure statistics of satellite components, most failures are attributed to the actuators of the attitude and control system (AOCS), such as the RW motor [23]. Therefore, the proposed method was implemented to monitor the health and predict the degradation of the RW motor to improve their reliability.

Few studies have addressed the prognostics of RW motors [24, 25]; however, motor RUL prediction is conducted at the single-component level. Motivated by the aforementioned limitations and requirements, this case study addresses the RUL prediction of an RW motor based on the proposed system-level prognostics framework. In this study, we conducted an accelerated life test (ALT) on an RW motor for a period of 3 years to acquire real measurement data with a low sampling rate, similar to a space environment. A proper failure threshold was imposed on the motor based on the characteristic curve given by the design requirement. The RUL is predicted using the degradation relation between the system and its components, assuming that the data are obtained during space operations.

4.2 Experimental Setup

The RW in this study was developed for the Korean Space Launch Vehicle, named the Science and Technology Satellite-3 (STSAT-3), and is addressed in Ref. [26]. It is actuated by a motor to provide consistent angular momentum and control its precise attitude. ALT was performed for this motor; one operation cycle comprises a short-term pull-up followed by a longer period at constant speed. During ALT, the

current and angular velocity signals were acquired at a sampling rate of 2 Hz. The pull-up test lasts only for a few seconds, while the rest of the time is given for the constant-speed test which extends from 10 to 20 h. Consequently, a day is spent for a single-cycle operation, on average, and the entire test lasts for three years. The pull-up operation evaluates motor performance by applying maximum voltage to the motor. The test was conducted under two extreme temperature conditions, i.e., hot (60 °C) and cold (−30 °C), within a thermal vacuum chamber to evaluate its reliability and performance. Even after three years there were no failures, but the test was stopped considering safety and the abnormally high current consumption.

4.3 Application of the Systems Approach

4.3.1 Online Parameter Estimation

In online diagnosis, the EKF is used to estimate the health status based on the motor dynamic model and measured signals from each cycle. The governing equations for the mechanical and electrical parts of the motor are the same as those in Sect. 2. Table 3 lists the model parameters used in this case study. The health parameters responsible for the motor performance degradation are given by $\boldsymbol{h} = [k_T, b]^T$ which are the back EMF and friction coefficients, relating to the permanent magnet health and the bearing condition, respectively. The input operation parameter is the voltage V at current time t.

However, unlike the simulation studies, it is difficult to assign initial values to the process. Measurement of noise covariance and improper values significantly affect and degrade the performance. To overcome this, an Adaptive EKF (AEKF) was employed to adaptively estimate the covariance matrices at each step of the EKF [27]. The forgetting factor ($\alpha = 0.8$) is used for adaptive estimation. Note that a larger α indicates more weight on previous estimates and incurs less fluctuation in the covariance, as well as longer time delays to adapt to changes. In this study, $\alpha = 0.8$ for all studies.

Table 3 Parameter description and values for extended Kalman filter (EKF)

Symbol	Description	Value
R	Armature resistance	22 Ω
L	Armature inductance	0.1215 H
J	Moment of inertia	0.001143 kg m^2
b	Friction coefficient	1.01×10^{-5} N m s/rad
k_T	Electromechanical coupling coefficient	0.054 Nm/A
V	Input voltage	24 V
T_L	Load torque	0.0001 Nm

4.3.2 Motor System Performance

To evaluate the performance of the RW motor, a typical characteristic curve that is defined by the relation between the output torque ($T_{output} = J\dot{\omega}$) and the angular velocity ω during the pull-up range was applied. To ensure the minimum actuation performance of the RW, the motor must generate at least 5 Nm of output torque at $\omega^* = 314.16$ rad/s, i.e., the motor is considered to have failed when the performance falls below this point. This is a design requirement for the STSAT-3 mission, where a satellite with an inertial moment of 18 kg m^2 needs to maneuver 25° in 40 s. In this context, motor system performance is defined by the following expression:

$$P_{sys} = J\dot{\omega}|_{\omega=\omega^*}, \tag{14}$$

and the failure threshold point is given by 5 Nm.

4.3.3 Offline Prognosis and Monitoring

In the offline monitoring and prognosis, the health parameters $\boldsymbol{h}$, estimated from the online diagnosis for each cycle, were transferred and monitored until the current cycle. An empirical degradation model was introduced to quantitatively describe the health degradation over long-term cycles, in which the model parameters were estimated using the accumulated health parameters. A particle filter (PF) was used in this case study to recursively estimate the probability density function (PDF) of the long-term health status and model parameters in the form of particles [28, 29]. The future trend was predicted by extrapolating each particle to future cycles. As in the EKF, the standard PF also consists of the state transition function f and measurement function h, as follows:

$$x_k = f(x_{k-1}, \beta_k), \tag{15}$$

$$z_k = h(x_k, n_k), \tag{16}$$

where k is the cycle step index, x_k is the estimated health state, β_k is the degradation model parameter, z_k is the measurement data (in this case, the health parameter values obtained using the online estimation), and n_k is the measurement noise. To account for degradation, an empirical exponential function was employed for function f [30–32]:

$$f(x_{k-1}, \beta_k) = exp(\beta_k dt)x_{k-1}. \tag{17}$$

The Gaussian PDF assumes the measurement noise, $n_k \sim N(0, \sigma_k)$, where σ_k is the unknown standard deviation. Consequently, the unknown parameter to be estimated is $\theta = [x, \beta, \sigma]^T$. It should be emphasized that the health parameters are

estimated by the motor dynamic model using the AEKF for the online stage, whereas its trend over long-term cycles is estimated by the degradation model using the PF for the offline stage. Once the degradation model is estimated up to the current cycle, it is used to predict future RUL values.

In an offline prognosis, it is often the case that the degradation trend accelerates after a certain cycle or initial fault. To account for this in the PF process, a shifting kernel PF (SKPF) that can detect when the current cycle deviates from the normal is used [33]. To this end, SKPF calculates the likelihood L, and subsequently calculates the decision function d_k:

$$d_k = -\ln\left(\frac{1}{N}\sum_{i=1}^{N} L\left(z_k|x_k^i, \beta_k^i, \sigma_k^i\right)\right). \tag{18}$$

When the observed degradation is close to the normal condition, the likelihood tends to be high and assumes a negative value; therefore, degradation is not monitored. Conversely, when the state degrades in a different fashion, e.g., deviates from the normal, the likelihood becomes lower and assumes a positive value. By monitoring these cycles and examining when the decision function reaches a positive value, the anomaly point is identified. Once detected, the SKPF shifts the kernel function used in the resampling step of the PF and adapts to the new degradation trend.

4.4 Application Results

In this section, the results of applying the AEKF to the system framework are discussed. In the AEKF, the initial values are necessary; they are given as $\boldsymbol{x}_0 = \left[0, 0, 0.054, 10^{-5}\right]^T$ based on the motor specification, and the first two are the state variables $[\omega, i]^T$, whereas the remainder are the health parameters $[k_T, b]^T$, respectively. The initial process and measurement noise covariances were arbitrarily assumed as $Q = \left[10^{-5}\,0; 0\;10^{-5}\right]$ and $R = [2\;0; 0\;0.1]$, respectively. The value at the end of time is then used as the health value of the cycle.

The ALT test ended at 658 and 600 cycles under cold and hot conditions, respectively. Among the results, the degradation of the friction coefficient (b) under cold conditions was noticeable, while the others did not change significantly. Therefore, the test data under cold conditions were used in this study to verify the proposed methodology. Bearing degradation was found to be dominant in this test and was responsible for the motor performance degradation. This conforms to the literature, which indicate that the bearing is the most vulnerable in RW motors.

The characteristic curves obtained from the online diagnosis in each cycle are shown in Fig. 9a, where the x-axis represents the angular velocity, and the y-axis represents the output torque. The graph shows that the slope of the curve constantly decreases as the cycle proceeds and approaches the threshold point. Because the motor system performance is defined by the torque at $\omega^* = 314.14$ rad/s, it is marked

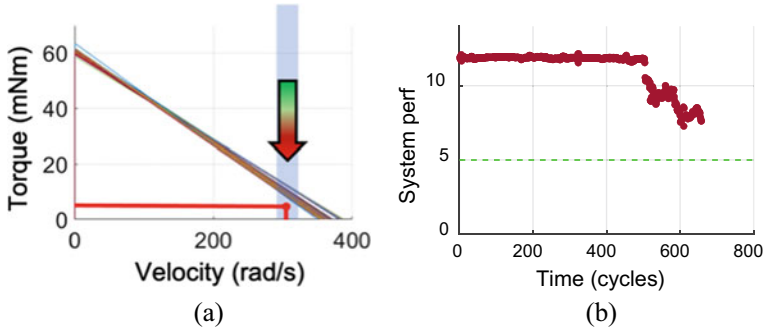

Fig. 9 **a** Characteristic curve and **b** system performance data of cold condition test

by the points in Fig. 9b; the green dashed line indicates the threshold. Even though the test lasted over three years with 658 cycles, the results indicate that the motor did not fail.

Using the data up to 658 cycles, the degradation models of each health parameter were estimated and their future was predicted using the SKPF. The results for both parameters are shown in Fig. 10a, c. The blue dots and triangles represent the estimated health values and anomaly points, respectively, detected by the decision function. The red dashed and solid lines represent the median and 95% PI, respectively. Figure 10b, d represent the trace of the anomaly decision function. The blue line with a circle represents the decision function value, and the red dotted line represents the anomaly threshold set by the user. The results of parameter b, as shown in Fig. 10c, confirm that SKPF successfully detects the initial point of the degradation trend change after 500 cycles. Few anomalies were detected before 500 cycles, which may be attributed to sudden abnormal measurements during normal conditions. When the degradation pattern changed after 500 cycles, the SKPF algorithm successfully adapted to the new degradation trend. The trace of the decision function shows that d_k increases significantly and exceeds the threshold when the estimated state becomes incoherent with the observed data.

On completion of prediction for future cycles, the health parameters are transferred to the online stage and used in the state model to predict the system performance. Subsequently, they are transferred to the offline stage. The results are shown in Fig. 10e with the median and 95% PI. With the system threshold given by the green dotted line, the EOL cycle for the system was predicted to be 808 cycles and the RUL was 150 cycles. It should be noted that the reason for predicting RUL at 658 cycles is that the test ended at this cycle. To validate this prediction, test should be continued further till 808 cycles; however, it was not conducted owing to limited cost and time.

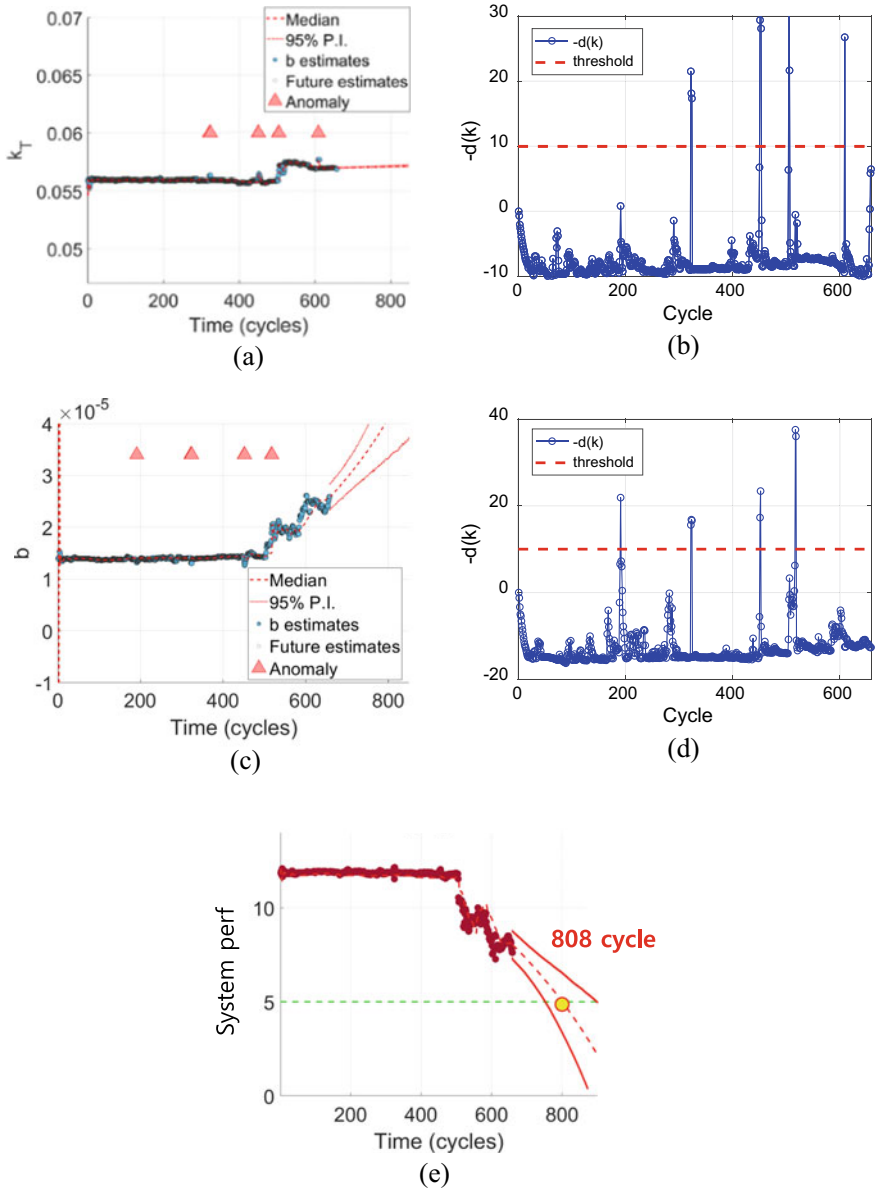

Fig. 10 **a** Prediction of parameter k_T by SKPF algorithm and **b** corresponding decision function **c** prediction of parameter b by SKPF algorithm and **d** corresponding decision function **e** prediction of system performance based on the health parameters

5 Case Study 2: Driving Motors in Quadcopters

5.1 Problem Definition

Since the commercial launch of quadcopters in early 2000s as unmanned aerial vehicles, their use, particularly in the field of aerial imaging, has been burgeoning [34]. Several commercial services related to agriculture activities, traffic control, and delivery of goods have been launched for quadcopters since the mid-2010s; however, safety issues owing to quadcopter failure have become a concern, with a high-risk failure factor being the occurrence of falls owing to the performance degradation of driving motors [35].

Based on a literature survey, it was found that most studies on the health diagnosis of quadcopter motors have been conducted to aid the design of robust flight controllers [36–38]. Therefore, they do not focus on health management or failure prevention based on the PHM framework. The recent studies in this direction that exploit parameters such as the vibration, current, or rotational speed have mainly been sensor-based approaches requiring attachment of additional sensors to the quadcopter [39–42].

The quadcopter can record various flight information, such as posture and angular velocity, position and linear velocity, and motor control data during flight. By exploiting these data and KF algorithms, it is possible to estimate the forces and moments acting on the aircraft and the degradation of the motor performance. In this case study, a PHM framework is presented that evaluates the health of individual motors and predicts their RUL based on the systems approach. It is applied to a Parrot Mambo drone (PMD), a micro quadcopter, to demonstrate the RUL prediction of the driving motors. Practically, the PMD structure is vulnerable to failure, and placing sensors to diagnose motor conditions is challenging. The PMD is more suitable for application of the framework proposed in this study.

5.2 Experimental Setup

The PMD used in this case study is a miniature quadcopter manufactured and sold by Parrot, France, measuring 7.1 $\times$ 7.1 inches and weighing 63 g [43]. The parameters for the PMD quadcopter dynamic analysis that were obtained using the MathWorks Simulink Parrot Minidrone model and actual measurements are summarized [44, 45]. The PMD is equipped with an 8520 coreless DC motor whose parameters were obtained from experiments based on the data from previous studies [46].

The overall framework for prognostics of quadcopter motor comprises two phases as shown in Fig. 11. The first step in online diagnosis is the state estimation of the quadcopter using a KF. The force and moment acting on the aircraft, as well as the rotational speed of the four motors were estimated using the flight data in the dynamics model of the quadcopter. The second step in the online diagnosis is the

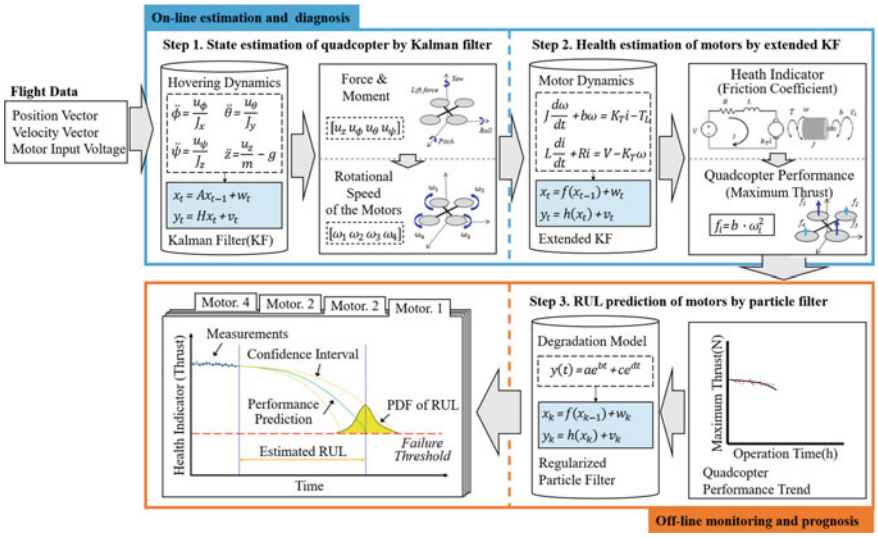

Fig. 11 The Quadcopter PHM framework

health estimation of motors using an EKF. The friction coefficient representing the degree of motor degradation was estimated by applying the estimated rotational speed of each motor to its dynamic model. Consequently, thrust, which represents a HI of the motor, was obtained. Offline observations identify the decreasing trend of thrust in each motor over long-term cycles and predict the RUL until failure. To realize this, an empirical degradation model was introduced, and the RUL of each motor was predicted using a regularized PF (RPF). Here, failure is defined as a situation in which the quadcopter cannot hover, i.e., it cannot sustain its own weight during lift-off.

5.3 Application of the Systems Approach

5.3.1 State Estimation of Quadcopter Using KF

The first step in online diagnosis involves the application of flight data collected during hovering to the quadcopter dynamics model to estimate the force and moment applied to the aircraft. The rotational speeds generated by the motors are estimated based on data obtained from hovering flights in this study. During hovering, there are nearly no roll, pitch, or yaw motions to maintain posture. Consequently, the equations for the translational and rotational degrees of freedom are obtained as follows:

$$\ddot{z} = \frac{u_z}{m} - g, \ddot{\phi} = \frac{u_\phi}{J_x}, \ddot{\theta} = \frac{u_\theta}{J_y}, \ddot{\psi} = \frac{u_\psi}{J_z} \tag{19}$$

In this equation, the vector $[z\ \phi\ \theta\ \psi]^T$ denotes the altitude z and rotational angles, i.e., the roll, pitch, and yaw motions, respectively, and its 2nd derivative $\left[\ddot{z}\ \ddot{\phi}\ \ddot{\theta}\ \ddot{\psi},\right]^T$ is the vertical acceleration and corresponding rotational-angular accelerations, respectively. The vector $\left[m\ J_x\ J_y\ J_z\right]^T$ is the mass and rotational inertia, and g is the gravitational acceleration. The vector $\left[u_z\ u_\phi\ u_\theta\ u_\psi\right]^T$ is the vertical force and moment acting on the quadcopter aircraft.

The flight data collected during hovering are the position vector $[z\phi\ \theta\ \psi]^T$ and its derivative: the velocity vector $\left[\dot{z}\ \dot{\phi}\ \dot{\theta}\ \dot{\psi},\right]^T$. By applying these to (19), the vector of the vertical force and moments $\left[u_z\ u_\phi\ u_\theta\ u_\psi\right]^T$ can be estimated. To implement this, a KF in which the system and measurement models are defined in recursive form, is applied [47]. Once the force and moments are obtained, the rotational speed ω_i of each motor can be obtained as follows [48].

$$\begin{bmatrix} \omega_1^2 \\ \omega_2^2 \\ \omega_3^2 \\ \omega_4^2 \end{bmatrix} = \begin{bmatrix} \frac{1}{4c} & \frac{-1}{4cl} & \frac{-1}{4cl} & \frac{-1}{4d} \\ \frac{1}{4c} & \frac{-1}{4cl} & \frac{1}{4cl} & \frac{1}{4d} \\ \frac{1}{4c} & \frac{1}{4cl} & \frac{1}{4cl} & \frac{-1}{4d} \\ \frac{1}{4c} & \frac{1}{4cl} & \frac{-1}{4cl} & \frac{1}{4d} \end{bmatrix} \begin{bmatrix} u_z \\ u_\phi \\ u_\theta \\ u_\psi \end{bmatrix} \tag{20}$$

where ω_i are the rotational speed of each motor, respectively; c is the motor thrust coefficient; l is the length of the arm; and d is the motor drag coefficient. The motor thrust f_i is proportional to the square of the speed ω_i^2 and is expressed as follows:

$$f_\mathrm{i} = c \cdot \omega_\mathrm{i}^2 \tag{21}$$

5.3.2 Health Estimation of Motors by Extended KF

In the second step of the online diagnosis, the friction coefficient of each motor was estimated by applying the estimated rotation speed of the motor to its dynamic model. The motor dynamic model comprises the same governing equations as the physics-based approach described in Sect. 2. When a cycle lasts for an extended period, performance degradation of the motor occurs due to various factors. The most representative is an increase of frictional force owing to wear of mechanical parts, such as bearings or brushes, which corresponds to coefficient b [49].

Once the motor friction coefficient b is estimated using the EKF, it can be directly used as a health indicator. However, it is preferable to use the maximum thrust under the corresponding degraded condition. This is because the quadcopter fails when the sum of the maximum thrust of the four motors is lower than the thrust required to maintain the takeoff and hovering of the quadcopter. By exploiting this in the prognosis, RUL can be predicted using this as a failure threshold. The threshold can be calculated using the following formula:

$$F_{hov} = m(g + a) + f_d,\ f_d = C_d \frac{1}{2} \rho v^2 A \tag{22}$$

where F_{hov} is the thrust required for hovering, m is the mass of the quadcopter, g is the acceleration due to gravity, a is the takeoff acceleration, f_d is the drag force, C_d is the drag coefficient, ρ is the air density, v is the takeoff speed, and A is the cross-sectional area of the quadcopter in the horizontal plane [44]. The maximum thrust of the motor is obtained by calculating the rotation speed using the motor dynamic model under the current value of the friction coefficient at the maximum input voltage condition and applying it to (21).

5.3.3 RUL Prediction of Motors by PF

The maximum thrust of the motor decreases with each cycle as the motor performance degrades due to the increase in mechanical friction. During offline monitoring, these cycle trends are monitored in two stages. First, the anomaly detection which detects the cycle at which a deviation occurs from the normal condition due to fault development. Next, the degradation prediction after anomaly detection in which the thrust begins to decrease exponentially as the cycle continues. The degradation trend is suitably described by introducing an empirical model and RUL until failure is predicted.

In this study, the anomaly is detected by the Naïve Bayes classifier which explores the first prediction time (FPT), i.e., the cycle point where the normal and fault conditions are divided [50]. Once the anomaly is detected, it is presumed that the degradation begins to increase, and an empirical degradation model is employed to describe this trend. The PF algorithm is used to estimate the model parameters and predict the RUL, similar to that of *Case study 1*.

5.4 Application Results

5.4.1 Online Estimation and Diagnosis of the PMD Motors

As the first step of online diagnosis, the KF is used to estimate the rotational speed of each motor during 5–50 s of hovering motion. In the KF, the standard deviations of the process and measurement noises are given by 0.1 and 1×10^{-5}, respectively. The mean values are 1809.12, 1809.12, 1809.12, and 1809.11 rad/s, and the rotational speeds are nearly identical to maintain a stationary posture during hovering. To calculate the maximum thrust as the second step of the online diagnosis, the motor friction coefficient was first estimated using the dynamic model of the motor and EKF. The results are shown in Fig. 12. The standard deviations of the process and measurement noises were 1×10^{-13} and 1×10^{-3}, respectively. As is evident from these figures, the friction coefficient rapidly converges to a constant value, although it

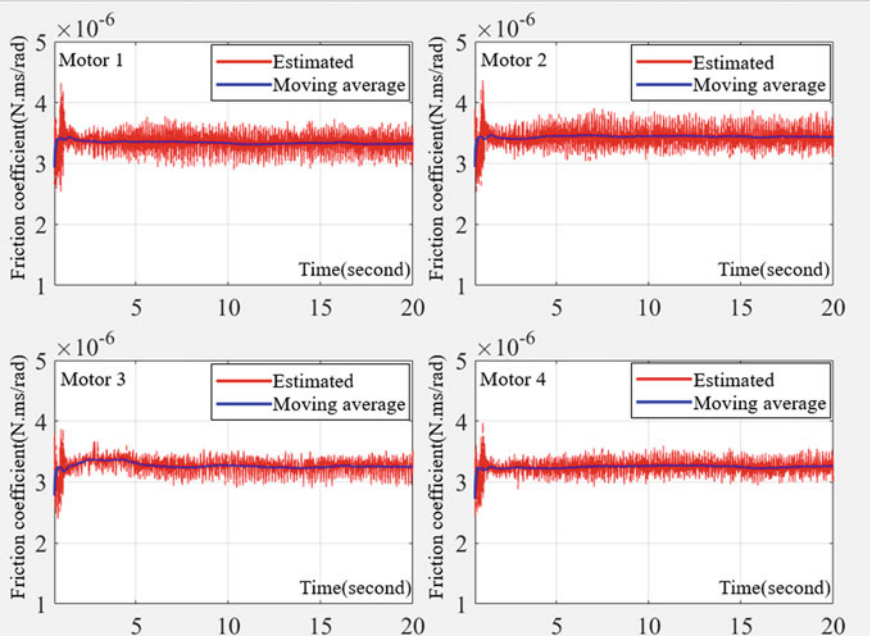

Fig. 12 Friction coefficient of motors during PMD hovering

tends to fluctuate around the mean, which is 3.31×10^{-6}, 3.43×10^{-6}, 3.27×10^{-6}, and 3.25×10^{-6}, respectively. The maximum thrust of each motor can be obtained by applying the maximum input voltage, which was 2.7 V in this case. After passing through the motor dynamic model under this condition and the friction coefficient of each motor, the rotational speeds were obtained as 2217, 2199, 2224, and 2226 rad/s. Consequently, the maximum thrust becomes 0.232, 0.2282, 0.2335, and 0.2339 N, respectively, according to (21).

5.4.2 Offline Monitoring and Prognosis

To implement the RUL prediction of the PMD motors, Motor 4 was chosen to perform accelerated degradation until failure occurred, which occurred after 106 h. During degradation, 48 cycles of hovering tests were performed at intermittent intervals and flight data were collected. The target was that the altitude should be maintained at 1.1 m with a rotational angle of 0 rad during the hovering mode. The RUL of Motor 4 was predicted using the RPF. The failure threshold of the PMD was determined as $0.2224N$ using (22). In the calculation, a is 2.5 m/s^2, f_d is 0.0776 N, C_d is 0.0624, ρ is 1.225 kg/m^3, v is 2.5m/s, and A is 0.325m^3.

The maximum thrust was obtained by the KF-based online estimation at each cycle for the motors until the 48th cycle. Figure 13 shows the results for Motor 1

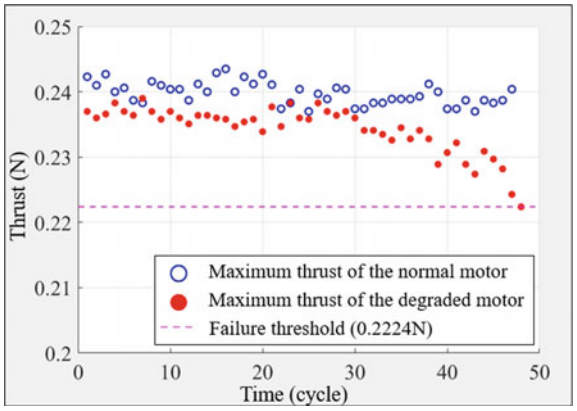

Fig. 13 Online estimation of maximum thrust at each cycle

(normal) and Motor 4 (degraded), and it can be observed that Motor 1 maintains a maximum thrust value between 0.2435 and 0.237 N, whereas Motor 4 gradually degrades after approximately 30 cycles.

Two exponential functions were employed for the RPF degradation model as follows.

$$f = \beta_1 exp(\beta_2 t) + \beta_3 exp(\beta_4 t) \tag{23}$$

where f is the maximum thrust of the motor, t is the long-term cycle index (don't be confused with the time in on-line diagnosis), and $\beta_i (i = 1, \ldots, 4)$ are the parameters in the degradation model.

$$x_0 \sim U(0.23, 0.25), \beta_2 \sim U(0.10, 0.15), \beta_3 \sim U(0.2, 0.3),$$
$$\beta_4 \sim U(-0.1, 0.0), and\, \sigma \sim U(0, 0.01).$$

From these, 3000 particles were generated for use in the subsequent process, and the thrust at the current cycle as well as the future values were predicted recursively using the RPF. Figure 14 shows the RUL prediction performed at 39 cycles. The filled and empty black dots represent the data collected up to the current and future cycles until failure, respectively. The red dashed and dotted lines after 39 cycles illustrate the median and 90% PI of the future thrust prediction. The magenta-colored horizontal line represents the failure threshold, and the black vertical line represents the anomaly point. The prediction results show excellent performance because the true EOL resides within the PI and is close to the median of the predicted distribution.

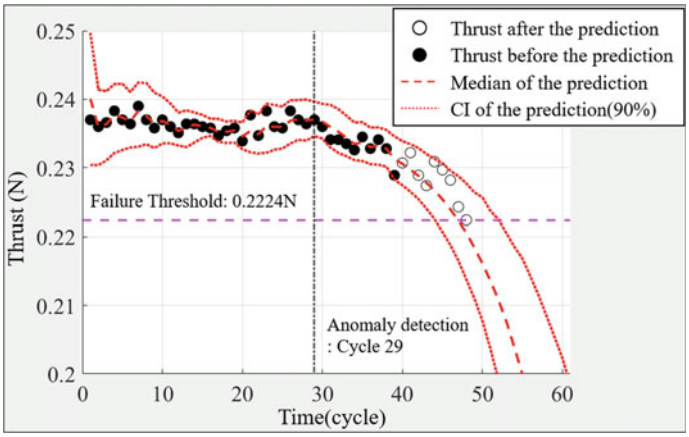

Fig. 14 RUL prediction at cycle 39

6 Conclusion

In this study, a system framework that takes advantage of the motor dynamics and KF estimation was presented to conduct the PHM of DC motors using a model-based approach. Most previous studies treat the motor as a single component and used a data-driven approach in which the raw signal of electric current or vibration was extracted and used for RUL prediction. However, in this study, the motor was considered as a system with multiple components; the health of the components was estimated individually, from which the RUL with respect to the motor system performance was predicted. In the literature, the degradation model for the system was typically used to predict future behavior. However, in this study, it was not introduced but obtained because of component degradation. The proposed framework is validated using two case studies, that is, a satellite RW and the driving motors of a quadcopter. The results demonstrate that the proposed method can provide an effective means to aid decision making in practical applications for DC motors.

Several benefits are expected from this approach; however, we do not have to generate an enormous volume of run-to-fail data for training the data-driven models because we employed the model-based approach. The approach can also be applied in a straightforward manner to other types of motors, provided that the associated model parameters are available or measured a priori. This is in contrast to the data-driven approach, which requires training whenever a motor is changed.

Acknowledgements This research was supported by the National Research Foundation of Korea (NRF) grant funded by the Korean government (MSIT) (No. 2020R1A4A4079904) and the MOTIE (Ministry of Trade, Industry, and Energy) in Korea, under the Fostering Global Talents for Innovative Growth Program (P0017307) supervised by the Korea Institute for Advancement of Technology (KIAT). In addition, we would like to thank Editage (www.editage.co.kr) for English language editing.

References

1. Lee J, Wu F, Zhao W, Ghaffari M, Liao L, Siegel D (2014) Prognostics and health management design for rotary machinery systems—Reviews, methodology and applications. Mech Syst Signal Process 42(1–2):314–334
2. Sun B, Zeng S, Kang R, Pecht MG (2012) Benefits and challenges of system prognostics. IEEE Trans Reliab 61(2):323–335
3. Lessmeier C, Kimotho JK, Zimmer D, Sextro W (2016) Condition monitoring of bearing damage in electromechanical drive systems by using motor current signals of electric motors: a benchmark data set for data-driven classification. In: PHM Society European conference, vol 3, No 1
4. Li N, Zhou R, Hu Q, Liu X (2012) Mechanical fault diagnosis based on redundant second generation wavelet packet transform, neighborhood rough set and support vector machine. Mech Syst Signal Process 28:608–621
5. Kliman GB, Koegl RA, Stein J, Endicott RD, Madden AM (1988) Noninvasive detection of broken rotor bars in operating induction motors. IEEE Trans Energy Convers 3(4):873–879
6. Grubic S, Aller JM, Lu B, Habetler TG (2008) A survey on testing and monitoring methods for stator insulation systems of low-voltage induction machines focusing on turn insulation problems. IEEE Trans Industr Electron 55(12):4127–4136
7. Nandi S, Toliyat HA, Li X (2005) Condition monitoring and fault diagnosis of electrical motors—A review. IEEE Trans Energy Convers 20(4):719–729
8. Su H, Chong KT (2007) Induction machine condition monitoring using neural network modeling. IEEE Trans Ind Electron 54(1):241–249
9. Zidani F, Benbouzid MEH, Diallo D, Naït-Saïd MS (2003) Induction motor stator faults diagnosis by a current Concordia pattern-based fuzzy decision system. IEEE Trans Energy Convers 18(4):469–475
10. Martínez-Morales JD, Palacios E, Campos-Delgado DU (2010) Data fusion for multiple mechanical fault diagnosis in induction motors at variable operating conditions. In: 2010 7th International conference on electrical engineering computing science and automatic control. IEEE, pp 176–181
11. Wen L, Li X, Gao L, Zhang Y (2017) A new convolutional neural network-based data-driven fault diagnosis method. IEEE Trans Industr Electron 65(7):5990–5998
12. Gangsar P, Tiwari R (2020) Signal based condition monitoring techniques for fault detection and diagnosis of induction motors: a state-of-the-art review. Mech Syst Signal Process 144:106908
13. Kim S, Kim NH, Choi JH (2021) A study toward appropriate architecture of system-level prognostics: physics-based and data-driven approaches. IEEE Access 9:157960–157972
14. Kim S, Choi JH, Kim NH (2021) Challenges and opportunities of system-level prognostics. Sensors 21(22):7655
15. Rahimi A, Kumar KD, Alighanbari H (2017) Fault estimation of satellite reaction wheels using covariance based adaptive unscented Kalman filter. Acta Astronaut 134:159–169
16. El Sayed W, Abd El Geliel M, Lotfy A (2020) Fault diagnosis of PMSG stator inter-turn fault using extended Kalman filter and unscented Kalman filter. Energies 13(11):2972
17. Singleton RK, Strangas EG, Aviyente S (2014) Extended Kalman filtering for remaining-useful-life estimation of bearings. IEEE Trans Industr Electron 62(3):1781–1790
18. Zhu X, Zhang H, Xi J, Wang J, Fang Z (2015) Robust speed synchronization control for clutchless automated manual transmission systems in electric vehicles. Proc Inst Mech Eng Part D: J Autom Eng 229(4):424–436
19. Salem T, Haskew TA (1995) Simulation of the brushless DC machine. In: Proceedings of the twenty-seventh southeastern symposium on system theory. IEEE, pp 18–22
20. Bavdekar VA, Deshpande AP, Patwardhan SC (2011) Identification of process and measurement noise covariance for state and parameter estimation using extended Kalman filter. J Process Control 21(4):585–601

21. Park HJ, Kim S, Lee J, Kim NH, Choi JH (2022) System-level prognostics approach for failure prediction of reaction wheel motor in satellites. Adv Space Res. https://doi.org/10.1016/j.asr.2022.11.028
22. Hu D, Sarosh A, Dong YF (2012) A novel KFCM based fault diagnosis method for unknown faults in satellite reaction wheels. ISA Trans 51(2):309–316
23. Ji XY, Li YZ, Liu GQ, Wang J, Xiang SH, Yang XN, Bi YQ (2019) A brief review of ground and flight failures of Chinese spacecraft. Prog Aerosp Sci 107:19–29
24. Muthusamy V, Kumar KD (2022) Failure prognosis and remaining useful life prediction of control moment gyroscopes onboard satellites. Adv Space Res 69(1):718–726
25. Rahimi A, Kumar KD, Alighanbari H (2020) Failure prognosis for satellite reaction wheels using Kalman filter and particle filter. J Guid Control Dyn 43(3):585–588
26. Kim DH, Yang S, Cheon DI, Lee S, Oh HS (2010) Combined estimation method for inertia properties of STSAT-3. J Mech Sci Technol 24(8):1737–1741
27. Akhlaghi S, Zhou N, Huang Z (2017) Adaptive adjustment of noise covariance in Kalman filter for dynamic state estimation. In: 2017 IEEE power & energy society general meeting. IEEE, pp 1–5
28. An D, Choi JH, Kim NH (2013) Prognostics 101: A tutorial for particle filter-based prognostics algorithm using Matlab. Reliab Eng Syst Saf 115:161–169
29. Orchard ME, Vachtsevanos GJ (2009) A particle-filtering approach for on-line fault diagnosis and failure prognosis. Trans Inst Meas Control 31(3–4):221–246
30. Barbieri F, Hines JW, Sharp M, Venturini M (2015) Sensor-based degradation prediction and prognostics for remaining useful life estimation: validation on experimental data of electric motors. Int J Progn Health Manage 6(3):1–20. https://doi.org/10.36001/ijphm.2015.v6i3.2285
31. Bejaoui I, Bruneo D, Xibilia MG (2020) A data-driven prognostics technique and rul prediction of rotating machines using an exponential degradation model. In: 2020 7th International conference on control, decision and information technologies (CoDIT), vol 1. IEEE, pp 703–708
32. Yang F, Habibullah MS, Shen Y (2021) Remaining useful life prediction of induction motors using nonlinear degradation of health index. Mech Syst Signal Process 148:107183
33. Kim S, Park HJ, Choi JH, Kwon D (2020) A novel prognostics approach using shifting kernel particle filter of Li-ion batteries under state changes. IEEE Trans Ind Electron 68(4):3485–3493
34. Air & Space Magazine (2017) A brief history of quadrotors. Available https://www.smithsonianmag.com/air-space-magazine/brief-history-quadrotors-180963372/
35. Susini A (2015) A technocritical review of drones crash risk probabilistic consequences and its societal acceptance. RIMMA risk information management, risk models, and applications. LNIS 7:27–38
36. Zhong Y, Zhang Y, Zhang W, Zuo J, Zhan H (2018) Robust actuator fault detection and diagnosis for a quadrotor UAV with external disturbances. IEEE Access 6:48169–48180
37. Avram RC, Zhang X, Muse J (2017) Quadrotor actuator fault diagnosis and accommodation using nonlinear adaptive estimators. IEEE Trans Control Syst Technol 25(6):2219–2226
38. Asadi D, Ahmadi K, Nabavi SY (2022) Fault-tolerant trajectory tracking control of a quadcopter in presence of a motor fault. Int J Aeronaut Space Sci 23(1):129–142
39. Zahra N, Buldan RS, Nazaruddin YY, Widyotriatmo A (2021) Predictive maintenance with neural network approach for UAV propulsion systems monitoring. In: 2021 American control conference (ACC). IEEE, pp 2631–2636
40. Pourpanah F, Zhang B, Ma R, Hao Q (2018) Anomaly detection and condition monitoring of UAV motors and propellers. In: 2018 IEEE sensors. IEEE, pp 1–4
41. Kong W, Bian S, Li X, Wang C, Wang J (2021) A new integrated health management for quadrotors based on deep learning. In: 2021 IEEE 10th data driven control and learning systems conference (DDCLS). IEEE, pp 1418–1423
42. Darrah T, Kulkarni CS, Biswas G (2020) The effects of component degradation on system-level prognostics for the electric powertrain system of UAVs. In: AIAA Scitech 2020 forum, p 1626
43. Parrot, Mambo range documentation. Available https://www.parrot.com/en/support/documentation/mambo-range

44. MathWorks, fly a parrot minidrone using hover parrot minidrone simulink template. Available https://kr.mathworks.com/help/supportpkg/parrot/ug/fly-a-parrot-minidrone-using-the-hover-simulink-model.html#mw_7b5d113d-3c79-42eb-838d-c063463e5bb0
45. De Simone MC, Russo S, Ruggiero A (2015) Influence of aerodynamics on quadrotor dynamics. In: Recent researches in mechanical and transportation systems influence, pp 111–118
46. Karnavas YL, Chasiotis ID (2016) PMDC coreless micro-motor parameters estimation through grey wolf optimizer. In: 2016 XXII International conference on electrical machines (ICEM). IEEE, pp 865–870
47. Welch G, Bishop G (2006) An introduction to the Kalman filter. Technical report TR 95:041. Department of Computer Science University of North Carolina. NC, USA
48. Kaplan MR, Eraslan A, Beke A, Kumbasar T (2019) Altitude and position control of parrot mambo minidrone with PID and fuzzy PID controllers. In: 2019 11th international conference on electrical and electronics engineering (ELECO). IEEE, pp 785–789
49. Kulkarni CS, Corbetta M, Robinson EI (2021). Systems health monitoring: integrating FMEA into Bayesian networks. In: 2021 IEEE aerospace conference (50100). IEEE, pp 1–11
50. Wang G, Xiang J (2021) Remain useful life prediction of rolling bearings based on exponential model optimized by gradient method. Measurement 176:109161